

Heisenberg Spin Chains via Chalcogen Bonding: Noncovalent S×××O Contacts Enable Long-Range Magnetic Order

R Alex Mayo, Ian S Morgan, Dmitriy V Soldatov, Rodolphe Clérac, Kathryn E Preuss

▶ **To cite this version:**

R Alex Mayo, Ian S Morgan, Dmitriy V Soldatov, Rodolphe Clérac, Kathryn E Preuss. Heisenberg Spin Chains via Chalcogen Bonding: Noncovalent S×××O Contacts Enable Long-Range Magnetic Order. Inorganic Chemistry, 2021, 60 (15), pp.11338 - 11346. 10.1021/acs.inorgchem.1c01287 . hal-03339532

HAL Id: hal-03339532
https://hal.science/hal-03339532

Submitted on 9 Sep 2021

HAL is a multi-disciplinary open access archive for the deposit and dissemination of scientific research documents, whether they are published or not. The documents may come from teaching and research institutions in France or abroad, or from public or private research centers.

L'archive ouverte pluridisciplinaire **HAL**, est destinée au dépôt et à la diffusion de documents scientifiques de niveau recherche, publiés ou non, émanant des établissements d'enseignement et de recherche français ou étrangers, des laboratoires publics ou privés.

Heisenberg Spin Chains via Chalcogen Bonding: Noncovalent S···O Contacts Enable Long-Range Magnetic Order

R. Alex Mayo, Ian S. Morgan, Dmitriy V. Soldatov, Rodolphe Clérac,* and Kathryn E. Preuss*

Kathryn E. Preuss − *Department of Chemistry, University of Guelph, Guelph, Ontario N1G 2W1, Canada;* orcid.org/0000-0003-2342-5346; Email: kpreuss@uoguelph.ca

Rodolphe Clérac − *Univ. Bordeaux, CNRS, Centre de Recherche Paul Pascal, UMR 5031, F-33600 Pessac, France;* orcid.org/0000-0001-5429-7418; Email: clerac@crpp-bordeaux.cnrs.fr

R. Alex Mayo − *Department of Chemistry, University of Guelph, Guelph, Ontario N1G 2W1, Canada*

Ian S. Morgan − *Department of Chemistry, University of Guelph, Guelph, Ontario N1G 2W1, Canada*

Dmitriy V. Soldatov − *Department of Chemistry, University of Guelph, Guelph, Ontario N1G 2W1, Canada;* orcid.org/0000-0002-2101-8010

The new radical ligand 5,8-dimethyl-1,4-dioxonaphtho[2,3-*d*][1,2,3]dithiazolyl (**1**) is reported. Two crystal polymorphs, **1*α*** and **1*β***, differing in their pancake-bonded dimerization motif and S···O contact network, are identified. The self-assembly of Mn(II) metal ions with **1** leads to the formation of $[\mathbf{Mn(hfac)_2}]_3\mathbf{(1)_2}$ that exhibits a Mn(II)−radical−Mn(II)−radical−Mn(II) linear arrangement of three $Mn(hfac)_2$ units bridged by two radical ligands (hfac = 1,1,1,5,5,5-hexafluoroacetylacetonato-). Characterization by single-crystal X-ray diffraction of this Mn(II) complex packing structure reveals close noncovalent S···O contacts between the $[\mathbf{Mn(hfac)_2}]_3\mathbf{(1)_2}$ units in one dimension along the *b*−*c* direction. The magnetic properties of the coordination complex are characterized by dc and ac susceptibility measurements on a microcrystalline solid. The magnetic data down to 4.8 K indicate the presence of effective ferromagnetic interactions (J/k_B = +0.16 K) between the molecular S_T = 13/2 units along the supramolecular chain involving noncovalent S···O contacts. Below 2.9 K, a non-zero out-of-phase component appears in the ac susceptibility, indicating the presence of a three-dimensional magnetic phase transition.

Noncovalent interactions play a major role in the self-assembly of molecules in liquid media and in the solid state. The structure and function of proteins and DNA,[1] molecular recognition in biological systems,[2] and the physical properties of molecular solids[3] all have a crucial dependence on noncovalent interactions. Because strong intermolecular interactions, which are fundamentally Coulombic in nature, can have a deciding influence on both the structure and the function of molecular systems, their study is an important and growing field. Recently, the concept of σ-hole bonding has gained traction for describing a specific subset of intermolecular Coulombic interactions.[4]

By defining and mapping the surface electrostatic potential of a molecule, we find areas of positive potential, termed σ-holes, can be located along the extension of a Y−X covalent bond, where Y is an electron-rich group and X is a polarizable element (typically a heavier element belonging to groups IV−VII of the periodic table). A directional noncovalent interaction between a σ-hole and a negatively charged or electron-rich site of a neighboring molecule constitutes a σ-hole bond. While hydrogen bonding is arguably an example of σ-hole bonding,[5] halogen bonding provides a classic example of σ-hole bonding, where X is a halogen (not including F).[4b,6] Likewise, so-called chalcogen bonding[7] is clearly understood in the context of σ-hole bonding.[8] A molecular species with a divalent chalcogen atom (R_1−E−R_2, where E is some chalcogen, not including oxygen) exhibits two σ-holes on E, along the extension of each R−E bond.[7a,b]

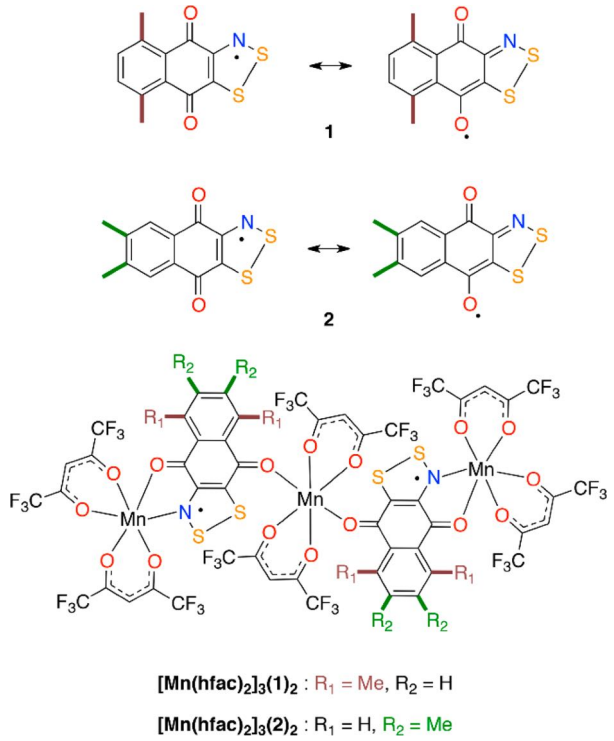
The geometric preferences and energetic contributions of H-bonds, and more recently halogen bonds, have been well-studied, and their importance in supramolecular chemistry is widely recognized.[3,5b,6] The role of noncovalent sulfur···oxygen interactions is increasingly identified as an important factor in the folding of proteins[9] and the conformation of molecules with biological activity.[10] As a result, study of the geometric preferences and energetic contributions of S···O interactions is being revisited. We have contributed to this field, reporting several instances in which noncovalent S···O contacts between paramagnetic species contribute to the remarkable magnetic properties of a crystalline solid.[11] We have also recently reported the role of noncovalent S···O contacts in supporting the reversible crystal-to-crystal chiral resolution of a small, achiral organic molecule.[12]

In the context of paramagnetic molecular solids designed using thiazyl heterocycles, it has been noted that electrostatic contacts of the $S^{\delta+}\cdots X^{\delta-}$ type (i.e., σ-hole bonds) may play a role in deterring the formation of so-called pancake bonds,[13] thereby supporting the formation of paramagnetic rather than diamagnetic materials.[14] Like other planar organic radicals,

many thiazyl radicals exhibit a propensity for the formation of a multicentered/two-electron (mc/2e) covalent bond via overlap of large portions of the singly occupied molecular orbitals (SOMOs) of neighboring molecules.[13] The contribution of such pancake bonds to the lattice enthalpy can be as large as that of H-bonds.[15] Providing a competing interaction in the form of $S^{\delta+}\cdots X^{\delta-}$ σ-hole bonding may be a method of delivering a paramagnetic molecular solid.

Herein, we report the synthesis of a new radical ligand, 5,8-dimethyl-1,4-dioxonaphtho[2,3-*d*][1,2,3]dithiazolyl [**1** (Chart 1)], a modification of our 6,7-dimethyl-1,4-dioxonaphtho[2,3-*d*][1,2,3]dithiazolyl (**2**).[16] The position of the methyl groups in **1** creates steric demands that are different from those of **2**, resulting in polymorphism of **1**, which is not observed for **2**. Moreover, the steric influence of the methyl group placement causes subtle differences in the supramolecular arrangement in coordination complexes of the two ligands, illustrated by comparing $[\mathbf{Mn(hfac)_2}]_3\mathbf{(1)_2}$ and the related $[\mathbf{Mn(hfac)_2}]_3\mathbf{(2)_2}$. A slight shift in the geometries of intermolecular interactions favors S···O contacts over competing S···S contacts (related to pancake bonding) and results in a dramatic difference in magnetic behavior. While $[\mathbf{Mn(hfac)_2}]_3\mathbf{(2)_2}$ exhibits antiferromagnetic (AF) coupling between paramagnetic molecular S_T = 13/2 units,[16] $[\mathbf{Mn(hfac)_2}]_3\mathbf{(1)_2}$ complexes appear to be ferromagnetically coupled along a supramolecular one-dimensional arrangement. This sharp contrast in magnetic behavior underscores the importance and delicate interplay between competing contacts and steric forces.

Chart 1. Neutral Radical Ligands 1 and 2, Showing Major Resonance Contributors (top) and Mn(II) Coordination Complexes Based on 1 and 2 (bottom)



General Considerations. 1,4-Benzoquinone was purchased from Acros Organics. 2,5-Dimethylthiophene was purchased from Alfa Aesar. *m*-Chloroperoxybenzoic acid (mCPBA), Amberlyst A21 free base, $NaS{\cdot}9H_2O$, MnO_2, $SbPh_3$, and S_2Cl_2 were purchased from Sigma-Aldrich. $Br_{2(l)}$ was purchased from Fisher. $NH_{3(g)}$ was purchased from BOC Gas. All commercial reagents were used as received, with the exception of (i) 1,4-benzoquinone, which was purified by sublimation immediately before use, (ii) MnO_2, which was activated by being heated to 100 °C for a minimum of 24 h prior to use, and (iii) $SbPh_3$, which was recrystallized from acetonitrile. With the exception of ethanol, anhydrous solvents were dispensed using a Solvent Purification System (LC Technology Solutions Inc.) equipped with molecular sieves (3 Å), from solvent kegs filled by Caledon Laboratories. Anhydrous ethanol was purchased from Commercial Alcohols. $Mn(hfac)_2{\cdot}2THF$ was synthesized according to literature methods.[17] 5,8-Dimethyl-1,4-naphthoquinone was prepared using modifications of literature methods.[18] Where indicated, reactions performed under an $Ar_{(g)}$ atmosphere were achieved using standard Schlenk and glovebox techniques. IR spectra were recorded on a Nicolet 4700 FTIR spectrometer at 4 cm^{-1} resolution. NMR spectra were recorded on a Bruker Avance-300 spectrometer at ambient temperature. Elemental analyses were performed by MHW Laboratories (Phoenix, AZ).

2,5-Dimethylthiophene-1,1-dioxide. mCPBA (28.66 g, 165.7 mmol) was slowly added to 2,5-dimethylthiophene (8.0857 g, 72.071 mmol) in 250 mL of CH_2Cl_2 at 0 °C. The stirred reaction mixture was maintained at 0 °C for 6 h and then allowed to warm to ambient temperature. After the mixture had been stirred for 3 days, excess mCPBA was removed by filtration. The burgundy filtrate was cooled using an $EtOH/CO_{2(s)}$ bath and filtered a second time. Excess A21 resin was added to the filtrate and stirred until the solution turned yellow. The resin was removed by filtration, and the solvent was removed by evaporation, resulting in a yellow solid, which was then crystallized from MeOH. The resulting microcrystalline yellow product was dried *in vacuo*. Yield: 2.0842 g (14.471 mmol, 20%). ^{1}H NMR (300 MHz, $CDCl_3$, 25 °C): δ 6.267 (s, 2H), 2.101 (s, 6H).

5,8-Dimethyl-1,4-naphthoquinone. 2,5-Dimethylthiophene-1,1-dioxide (2.0842 g, 14.471 mmol) and freshly sublimed 1,4-benzoquinone (1.3078 g, 12.099 mmol) were stirred in 100 mL of $CHCl_3$. The reaction mixture was gently refluxed, being monitored by ^{1}H NMR. After 8 days, the reaction generating an SO_2-bridged unsaturated naphthalenedione intermediate reached 98% completion. The solvent was removed by flash distillation, and dry toluene (75 mL) was added to the resulting yellow oil, followed by excess activated MnO_2. The reaction mixture was refluxed overnight. The solution was filtered through a bed of Celite and washed with toluene until the filtrate ran colorless. The solvent was removed from the filtrate, leaving a yellow crystalline solid. Yield: 1.5982 g (8.5892 mmol, 78%). ^{1}H NMR (300 MHz, $CDCl_3$, 25 °C): δ 7.376 (s, 2H), 6.818 (s, 2H), 2.684 (s, 6H)

2,3-Dibromo-5,8-dimethyl-1,4-naphthoquinone. Under an $Ar_{(g)}$ atmosphere and in the absence of light, a solution of Br_2 (2.7432 g, 17.165 mmol) in CH_2Cl_2 (~10 mL) was added dropwise to an orange suspension of 5,8-dimethyl-1,4-naphthoquinone (1.5982 g, 8.5892 mmol) in 10 mL of CH_2Cl_2. The reaction mixture was allowed to stir in the dark for 3 days. The resulting red/brown solution was reintroduced to the light, and $Ar_{(g)}$ was bubbled through it, resulting in the evolution of a smokelike visible suspension of white particulate in the head gas space of the flask and precipitation of a yellow solid as the solvent was allowed to partially evaporate. The resulting thick, yellow slurry was filtered, and the solid was rinsed with a small amount of CH_2Cl_2. The filtrate was recovered, and additional $Ar_{(g)}$ was bubbled through it. This step was repeated until a yellow/orange paste remained, which was washed by being stirred in EtOH and re-collected by filtration. All filtration residues were combined and dried *in vacuo* overnight leaving a bright yellow crystalline material. Yield: 2.5155 g (7.3155 mmol, 85%). ^{1}H NMR (300 MHz, $CDCl_3$, 25 °C): δ 7.42 (s, 2H), 2.69 (s, 6H).

2-Amino-3-bromo-5,8-dimethyl-1,4-naphthoquinone. Under $Ar_{(g)}$, 2,3-dibromo-5,8-dimethyl-1,4-naphthoquinone (2.5155 g, 7.3155 mmol) and anhydrous EtOH (120 mL) were added to a reaction vessel fitted with a condenser. Ammonium hydroxide (14 M, 0.051 mol) was added, and a deflated balloon was attached atop the condenser. The solution was saturated with $NH_{3(g)}$, and then the system was sealed and brought to reflux. After 24 h, the brown/red solution was cooled and maintained at ∼40 °C with a water bath while $Ar_{(g)}$ was bubbled through it. Once the solvent had evaporated, the remaining orange powder was recrystallized in denatured EtOH. Yield: 1.5547 g (5.5529 mmol, 76%). FTIR (KBr, cm^{-1}): 3496 (m), 3382 (m), 2966 (w), 2924 (w), 1659 (m), 1639 (m, sh), 1618 (s), 1589 (s), 1547 (s), 1385 (s), 1367 (s), 1328 (m), 1236 (s), 1123 (w), 1071 (m), 996 (w), 826 (w), 785 (w), 755 (m), 743 (w, sh), 693 (w), 582 (w), 513 (w). ^{1}H NMR (300 MHz, $CDCl_3$, 25 °C): δ 7.38 (d, 1H), 7.29 (d, 1H), 5.45 (br s, 2H), 2.74 (s, 3H), 2.68 (s, 3H).

2-Amino-3-thioacetyl-5,8-dimethyl-1,4-naphthoquinone. 2-Amino-3-bromo-5,8-dimethyl-1,4-naphthoquinone (1.5547 g, 5.5529 mmol) was added to a degassed solution of water (65 mL)/EtOH (10 mL) and NaS·$9H_2O$ (2.666 g, 11.10 mmol). The reaction mixture was heated and stirred for 3 h. The resulting deep purple solution was cooled with an ice bath, and acetic anhydride was added until an orange/red solid precipitated, in a pH range of ∼4−6. The precipitate was collected by suction filtration and washed with water. The orange solid was dried *in vacuo*. Yield: 1.5280 g (5.5551 mmol, ∼100%). FTIR (KBr, cm^{-1}): 3489 (w), 3369 (m), 2965 (w), 2926 (w), 1702 (m), 1675 (w), 1608 (s), 1578 (m, sh), 1541 (m), 1379 (s), 1329 (s), 1261 (w, sh), 1238 (s), 1196 (w), 1117 (w), 1033 (w), 994 (w), 950 (w), 815 (w, sh), 799 (w), 763 (w), 701 (w), 619 (w), 594 (w).

5,8-Dimethyl-4,9-dioxo-naphtho[2,3-*d*]-1,2,3-dithiazol-2-ium Chloride. Under $Ar_{(g)}$, dry acetonitrile (50 mL) was added to 2-amino-3-thioacetyl-5,8-dimethyl-1,4-naphthoquinone (1.3842 g, 5.0323 mmol). S_2Cl_2 (2.05 mL, 25.5 mmol) was added to the reaction vessel via syringe. The reaction mixture was stirred and heated with a warm water bath for 2 h. The solution was allowed to cool to room temperature, resulting in an orange precipitate suspended in a deep red solution. The precipitate was collected using a fritted filter stick and washed with cold, dry acetonitrile. The orange/brown solid was dried *in vacuo* for 2 days. Yield: 1.2201 g (4.1019 mmol, 82%). FTIR (KBr, cm^{-1}): 2963 (w), 2917 (w), 2849 (w), 1685 (m), 1655 (m), 1648 (w), 1638 (w), 1618 (w), 1609 (w), 1545 (w), 1376 (m), 1318 (m), 1263 (w), 1222 (s), 1171 (w), 1101 (m), 1032 (w), 951 (w), 921 (w), 860 (w), 812 (m), 800 (m), 745 (w).

5,8-Dimethyl-naphtho[2,3-*d*]dithiazolyl-4,9-dione (1). Under $Ar_{(g)}$, a solution of $SbPh_3$ (0.7220 g, 2.045 mmol) in dry acetonitrile (30 mL) was cannulated into a vessel containing 5,8-dimethyl-4,9-dioxo-naphtho[2,3-*d*]-1,2,3-dithiazol-2-ium chloride (1.2130 g, 4.1019 mmol) dissolved in dry acetonitrile (60 mL). The solution turned purple/blue with a suspended solid and was stirred for 2 h and then filtered with a fritted filter stick. The blue/purple precipitate was dried under vacuum. Yield: 0.9688 g (3.693 mmol, 91%). Portions of 200−250 mg were sublimed under dynamic vacuum (6.0×10^{-2} Torr) on a programmable temperature-gradient tube furnace (135, 90, and 60 °C). Sublimation yields ∼30%. FTIR (KBr, cm^{-1}): 2969 (m), 2926 (s), 2852 (m), 1675 (s), 1655 (sh, w), 1603 (s), 1577 (w), 1571 (w), 1560 (w), 1550 (m), 1420 (m), 1376 (sh, m), 1368 (m), 1328 (m), 1292 (w), 1262 (w), 1222 (s), 1187 (sh, w), 1178 (w), 1106 (m), 1033 (w), 1004 (w), 939 (w), 910 (w), 827 (w), 814 (w), 771 (w), 745 (w), 629 (w), 526 (w), 497 (w). Anal. Calcd for $C_{12}H_8NO_2S_2$: C, 54.94; H, 3.0; N, 5.34. Found: C, 54.7; H, 3.2; N, 5.21. Solution EPR: 1:1:1 three-line pattern, g = 2.0093, a_N = 4.836 G. Cyclic voltammetry: $E_{1/2}^{(0/+1)}$ = 0.77 V, $\Delta E_{PP}^{(0/+1)}$ = 230 mV; $E_{1/2}^{(-1/0)}$ = −0.47 V, $\Delta E_{PP}^{(-1/0)}$ = 360 mV.

[Mn(hfac)$_2$]$_3$(1)$_2$. Under $Ar_{(g)}$, **1** (61.0 mg, 0.232 mmol) and Mn(hfac)$_2$·2THF (142.6 mg, 0.2325 mmol) were dissolved in toluene (350 mL) with slight heating generating an emerald green solution that turned orange over time. The solvent was removed by flash distillation, and the purple/blue residue collected. The crude material was sublimed under dynamic vacuum (10^{-5} Torr) on a programmable temperature-gradient tube furnace (115, 90, and 60 °C). Pale brown microcrystals were recovered under $Ar_{(g)}$. Yield: 46.5 mg (0.0241 mmol, 31%). FTIR (KBr, cm^{-1}): 3142 (w), 2963 (w), 2917 (w), 2849 (w), 1647 (s), 1602 (m), 1560 (m), 1541 (m), 1483 (s), 1466 (m), 1450 (w), 1397 (w), 1383 (w), 1368 (w), 1341 (w), 1260 (s), 1204 (s), 1149 (s), 1096 (w), 1033 (w), 949 (w), 922 (w), 847 (w), 803 (s), 782 (sh, m), 743 (w), 665 (s), 585 (m), 528 (w). Anal. Calcd for $C_{54}H_{22}F_{36}Mn_3N_2O_{16}S_4$: C, 33.57; H, 1.15; N, 1.45. Found: C, 33.41; H, 1.20; N, 1.43. Brown block crystals suitable for single-crystal X-ray diffraction were grown by sublimation under static vacuum at 10^{-6} Torr and 110 °C.

Cyclic Voltammetry (CV). Electrochemical data were collected at a scan rate of 100 mV/s, using Pt wire working, reference, and counter electrodes, with BASi Epsilon-EC Bioanalytical Systems, Inc., version 2.10.73_USB (2009). A 1.0 M solution of **1** and 0.05 M nBu$_4$NPF$_6$ in dry CH_2Cl_2 was prepared under an inert atmosphere. The fc/fc$^+$ couple was used as an internal standard [$E_{1/2}^{(fc/fc+)}$ = +460 mV vs SCE].[19]

Electron Paramagnetic Resonance (EPR). Solution EPR measurements were performed using an X-band Bruker EMX spectrometer at ambient temperature. A very dilute solution of **1** in dry CH_2Cl_2 was prepared and sealed under an argon atmosphere in a cell with a reservoir allowing for concentration adjustment. Spectral simulation was performed using WinSim software.[20]

Magnetic Measurements. Magnetic susceptibility measurements were performed on a Quantum Design SQUID MPMS-XL magnetometer and PPMS-II susceptometer housed at the Centre de Recherche Paul Pascal at temperatures between 1.8 and 400 K and dc magnetic fields ranging from −7 to 7 T. The ac magnetic susceptibility measurements were performed in an oscillating ac field of 1−6 Oe with frequencies between 1 and 10000 Hz in a zero dc field. The measurements were carried out on polycrystalline samples of [**Mn(hfac)$_2$**]$_3$(**1**)$_2$ (12.40 and 20.90 mg) introduced into a sealed polyethene bag (3 cm × 0.5 cm × 0.02 cm; typically, 33−40 mg) in a glovebox under a controlled atmosphere of argon to avoid any contact with air or water. Prior to the experiments, the field-dependent magnetization was measured at 100 K on each sample to detect the presence of any bulk ferromagnetic impurities. As expected for paramagnetic or diamagnetic materials, a perfectly linear dependence of the magnetization that extrapolates to zero at zero dc field was systematically observed; the samples appeared to be free of any ferromagnetic impurities. The magnetic susceptibilities were corrected for the sample holder and the intrinsic diamagnetic contributions.

Crystallography. Single crystals of **1*α*** (0.50 mm × 0.03 mm × 0.03 mm, grown by slow evaporation of a CH_3CN solution), **1*β*** (0.10 mm × 0.10 mm × 0.10 mm, grown by sublimation), and [**Mn(hfac)$_2$**]$_3$(**1**)$_2$ (0.33 mm × 0.06 mm × 0.02 mm, grown by sublimation) were studied at the University of Guelph X-ray Facility. Data were collected at 293 K for **1*α*** and **1*β*** and at 150 K for [**Mn(hfac)$_2$**]$_3$(**1**)$_2$ on a SuperNova single-crystal diffractometer equipped with Cu Kα and Mo Kα microfocus radiation sources (λ = 1.54184 and 0.71073 Å, respectively), an Atlas CCD detector, and a Cryojet low-temperature device. The unit cell parameters were calculated and refined using the entire data sets. Unit cell refinement and data reduction were carried out using CrysAlisPro software.[21] Absorption corrections were applied using the multiscan method. Structures were determined (direct methods) and refined (full-matrix least squares on F^2) using SHELXS[22] and SHELXL-2013.[23] All non-hydrogen atoms were refined with anisotropic thermal parameters. All H atoms were included in calculated positions and allowed to refine in riding-motion approximation with U_{iso} tied to the carrier atom.

Synthesis. Radical **1** is prepared from 5,8-dimethyl-1,4-naphthoquinone in five steps. Although 5,8-dimethyl-1,4-naphthoquinone is commercially available, its high cost and small quantities make it more practical to synthesize this starting material. Known procedures for the preparation of 5,8-dimethyl-1,4-naphthoquinone[24] using 1,2,4,5-hexatetrene are

unattractive as the latter is not commercially available and is challenging to make. An alternate strategy uses 1,1′-thiophene dioxides as a dienophile in a Diels–Alder reaction with a 1,4-benzoquinone to generate a 1,4-naphthoquinone.[18,25] However, yields of the desired product are typically poor owing to reattack of the dieneophile on the diene product to form anthroquinones, resulting in product mixtures. Typical literature procedures reflux the thiophene dioxide with the benzoquinone in high-boiling point solvents such as toluene[25a] and acetic acid.[25c] The sulfone bridge in the resulting unsaturated naphthalenedione backbone (Scheme S1) is thermally unstable above ∼70 °C; thus, sulfur dioxide is released, and the aromatic naphthoquinone is formed, which is now subject to reattack by unreacted thiophene dioxide. To circumvent the thermal decomposition, we use refluxing chloroform (∼62 °C) to prevent the reaction from proceeding beyond the formation of a sulfur dioxide-bridged unsaturated naphthalenedione, which is not subject to further reaction with the thiophene dioxide. The reaction can be monitored by ^{1}H NMR until completion, usually after 5–8 days. Once the reaction to the sulfur dioxide-bridged species has gone to completion, the solvent is removed by flash distillation, dry toluene is added, along with activated MnO_2,[26] and this is refluxed, removing the SO_2 and aromatizing the naphthalene backbone. In this way, 5,8-dimethyl-1,4-naphthoquinone is prepared in high yield and purity (Scheme S1).

To synthesize the 1,2,3-dithiazole (DTA) ring on the naphthoquinone backbone, a primary amine must be added to position 2. However, unlike many reactions with both *p*- and *o*-quinones, sodium azide (NaN_3) in an acidic environment does not produce the desired amine product. To achieve the necessary precursor, a modification of a literature procedure[27] to brominate 5,8-dimethyl-1,4-naphthoquinone at positions 2 and 3 is used. Reaction with ammonium hydroxide (NH_4OH) and gaseous ammonia then produces 2-amino-3-bromo-5,8-dimethyl-1,4-naphthoquinone. It is worth noting that a reflux in EtOH was chosen rather than following the literature recommendation to use the more toxic nitrobenzene as a solvent.[28] As the reaction of 2-amino-3-bromo-5,8-dimethyl-1,4-naphthoquinone with S_2Cl_2 does not result in a Herz-type[29] ring closure, an alternate method of constructing the 1,2,3-dithiazole ring is employed. A thioacetyl group is incorporated at position 3 via reaction with sodium sulfide nonahydrate followed by acetic anhydride. The resulting 2-amino-3-thioacetyl-5,8-dimethyl-1,4-naphthoquinone is reacted with excess S_2Cl_2 under mild conditions (<40 °C for 3 h), generating the dithiazolylium chloride, which is then reduced to generate neutral radical **1** (Scheme S1). Analytically pure **1** is readily obtained by sublimation.

The $[\mathbf{Mn(hfac)_2}]_3\mathbf{(1)}_2$ coordination complex is rather straightforwardly prepared by reaction of **1** with $Mn(hfac)_2(THF)_2$ and is the only observed product, regardless of the stoichiometry used. The complex sublimes readily to form dark brown block crystals.

Crystal Structure. Neutral radical **1** crystallizes in two forms that differ in the mode of dimerization (also known as pancake bonding). Form **1*α***, grown by slow evaporation of a CH_3CN solution, exhibits a red needle habit and adopts monoclinic space group $P2_1/n$. The two molecules in the asymmetric unit are pancake-bonded in a twisted cofacial motif characterized by an ∼90° rotation of the thiazyl rings with respect to one another (Figure 1). At 293 K, the shortest S···S contact is well within the sum of van der Waals radii, at

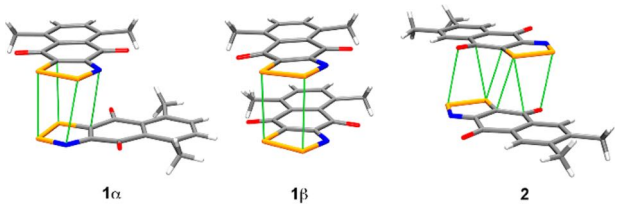


Figure 1. Excerpts from single-crystal structures illustrating pancake-bonded dimerization motifs. The asymmetric unit of **1*α*** (left) exhibits twisted cofacial dimerization with a single short S···S contact. One of six dimers of **1*β*** (middle) exemplifies a *cis*-cofacial dimerization with two short S···S contacts. The unusual dimerization of **2** (right) has no short S···S contacts (CSD Refcode ACOJAF).[16]

3.252(2) Å. Form **1*β***, grown by sublimation, exhibits a red-purple block habit and adopts triclinic space group $P\bar{1}$. This form is significantly more complex, with 12 molecules in the asymmetric unit, all pancake-bonded in a *cis*-cofacial motif (Figure 1) to form six dimers with S···S contacts ranging from 3.047(3) to 3.293(3) Å in length at 293 K. The positioning of the thiazyl rings relative to one another within a *cis*-cofacial dimer is distorted from the ideal value of 0°, exhibiting a rotation between ∼4° and ∼7°, likely owing to steric interference between methyl groups.

Interestingly, neither of the morphologies observed for **1** is reminiscent of the unusual pancake bonding observed in the 6,7-dimethyl-naphtho[2,3-*d*]dithiazolyl-4,9-dione, **2**,[16] in which short S···O contacts between sites of high spin density are dominant (Figure 1). Nevertheless, both **1*α*** and **1*β*** exhibit a complex network of lateral, noncovalent S···O contacts consistent in geometry with *σ*-hole bonding (Figures S1 and S2) and reminiscent of the S···O contacts observed in the structure of the related 1,2,3-dithiazolyl-*o*-naphthoquinone radical.[30]

Both the occurrence of polymorphism and the unusually high Z' of 12 observed in form **1*β*** are likely the result of competition between different types of noncovalent interactions, with the added steric interference of the methyl groups. As articulated by Steed and Steed in a recent review,[31] a high Z' can be viewed as a way of dealing with conflicting packing requirements by settling for an optimal balance of interactions, because no single molecular environment (i.e., $Z' = 1$) can satisfy all demands to form an optimal interaction with all neighbors. Chalcogen bonds impose requirements on the packing of molecules in the structure, and pancake bonding has particularly strict geometry requirements, as we have recently demonstrated.[32] Clearly, in **1**, methyl group placement hinders ideal molecular positioning for optimal overlap of SOMOs (Figure S3) in the pancake-bonded dimers while allowing optimal chalcogen bonding. The result is particularly evident in **1*β*** where pancake bonding geometries are unusually distorted or strained.

The molecular structure of $[\mathbf{Mn(hfac)_2}]_3\mathbf{(1)}_2$ is comparable to that of $[\mathbf{Mn(hfac)_2}]_3\mathbf{(2)}_2$ (CSD Refcode ACOHOR)[16] consisting of a central Mn(II) chelated by two equatorial hfac ligands and flanked by the two **1** radicals monodentate O-coordinated in the axial positions. Both radical ligands also chelate another $Mn(hfac)_2$ fragment, generating a Mn(II)–radical–Mn(II)–radical–Mn(II) trinuclear species (Chart 1 and Figure 2). The similarities and small differences in geometry and distance of noncovalent S···O and S···S short contacts in $[\mathbf{Mn(hfac)_2}]_3\mathbf{(1)}_2$ compared to $[\mathbf{Mn(hfac)_2}]_3\mathbf{(2)}_2$

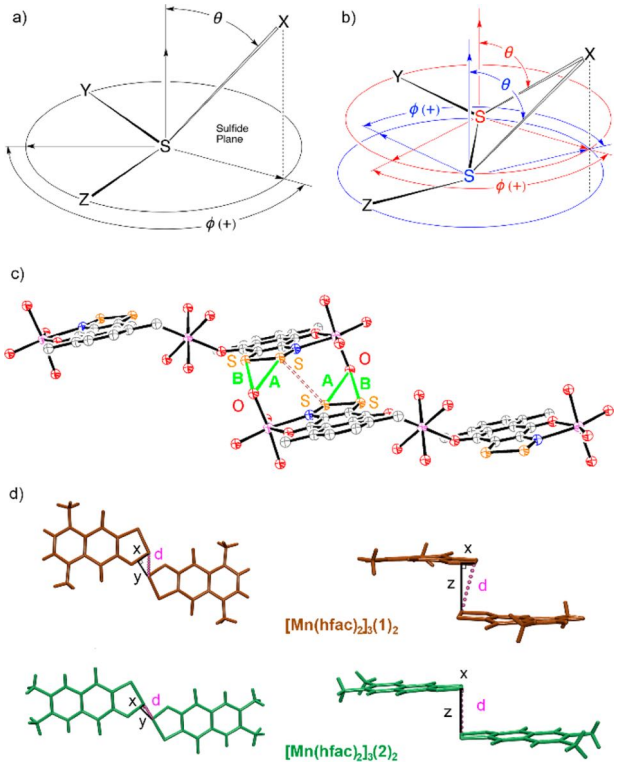


Figure 2. (a) Illustration defining angles θ and φ for the geometric characterization of nonbonding contacts with sulfides, adapted from ref 33. (b) Geometric characterization of a bifurcated nonbonding contact with a disulfide requires definition of two sulfide planes, as illustrated. (c) ORTEP illustration of the S···O and S···S contacts between neighboring molecules in $[\mathbf{Mn(hfac)_2}]_3\mathbf{(1)_2}$ (H atoms omitted; only O hfac atoms shown for the sake of clarity). (d) Excerpt from crystal structures of $[\mathbf{Mn(hfac)_2}]_3\mathbf{(1)_2}$ (brown) and $[\mathbf{Mn(hfac)_2}]_3\mathbf{(2)_2}$ (green) illustrating the *x*, *y*, and *z* parameters used for geometric characterization of S···S contacts (see Table 1).

are worth discussing in some detail, as these give rise to large differences in the magnetic properties (*vide infra*). Herein, we adapt Parthasarathy's pictorial model[33] to describe the distances and angles of short contacts with the S atoms of the disulfide part of the thiazyl ring (Figure 2). Parthasarathy et al. noted that, for a divalent sulfide, "electrophiles tend to approach S roughly 20° from the perpendicular to the plane ... whereas nucleophiles tend to approach approximately along the extension of one of the covalent bonds to S." Clearly, the observation regarding the preferred geometry of nucleophile approach describes σ-hole bonding and is relevant to S···O contacts. By contrast, S···S contacts should adopt geometries consistent with the approach of an electrophile, nearing a perpendicular approach for pancake bonding.

In both Mn coordination species, the relevant S···O contacts occur between an hfac O atom on a terminal $Mn(hfac)_2$ moiety and both S atoms of a thiazyl ring in a neighboring trinuclear molecule. These bifurcated (SS)···O contacts occur in a reciprocal fashion, illustrated in Figure 2c. Each Mn(II)−radical−Mn(II)−radical−Mn(II) unit participates in two reciprocal (SS)···O interactions, one at each terminus, resulting in a one-dimensional supramolecular arrangement of interacting $[Mn(hfac)_2]_3(radical)_2$ complexes along [011], as shown in Figure 3. The S···O contacts are electrostatic in nature, adopting a geometry consistent with σ-hole bond formation

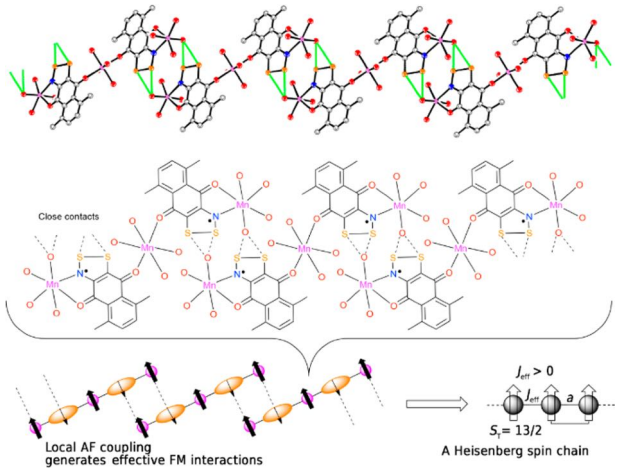


Figure 3. Reciprocal bifurcated (SS)···O contacts define chains of interacting complexes along the [011] direction. Local AF exchange coupling between Mn(II) centers and radical ligands generates an S_T = 13/2 ground state for an individual molecule. S···O contacts mediate local AF exchange coupling between Mn(II) centers and radical ligands on neighboring molecules, generating effective ferromagnetic (or ferromagnetic-like) interactions.

(Table 1). At 150 K, the geometry and distances of the (SS)···O interactions in $[\mathbf{Mn(hfac)_2}]_3\mathbf{(1)_2}$ are similar to those observed in $[\mathbf{Mn(hfac)_2}]_3\mathbf{(2)_2}$. This is an important observation because interactions of this nature are known to give rise to local antiferromagnetic interactions between $S = 5/2$ Mn(II) and radical ligand spins from neighboring trinuclear complexes (Figure 3). Overall, this type of heterospin (SS)···O contact generates an alignment of the $[\mathbf{Mn(hfac)_2}]_3\mathbf{(radical)_2}$ total spins, in other words an effective ferromagnetic interaction along the supramolecular chain as exemplified in the bottom part of Figure 3.[11]

A single short S···S contact occurs between neighboring molecules and involves the two closest S atoms within the same unit defined (*vide supra*) by the two reciprocal (SS)···O interactions (Figure 2). Importantly, at 150 K, the S···S contact distance of $[\mathbf{Mn(hfac)_2}]_3\mathbf{(1)_2}$ is markedly longer than that of $[\mathbf{Mn(hfac)_2}]_3\mathbf{(2)_2}$ [3.528(2) Å vs 3.388(2) Å]. Furthermore, the S···S contact geometry in $[\mathbf{Mn(hfac)_2}]_3\mathbf{(1)_2}$, characterized by parameters *x*, *y*, and *z* (Figure 2d and Table 1), differs significantly from that in $[\mathbf{Mn(hfac)_2}]_3\mathbf{(2)_2}$. This last observation is important because the S···S contact promotes AF coupling between thiazyl radical units, with the extreme case being pancake bonding. Keeping with the same contact scheme (Figure 2c), coordination complexes in which the S···S contact would be short, for example, $x \sim 0$ Å, $y \sim 0$ Å, and $z \sim 3$ Å, are likely to promote strong enough AF interactions to compensate for the effective ferromagnetic (SS)···O interactions. In the case presented here, *x* is particularly important because the small value of *x* of 0.21(1) Å in $[\mathbf{Mn(hfac)_2}]_3\mathbf{(2)_2}$ improves the orbital overlap between the π systems of neighboring radical ligands, compared to the larger *x* of 0.46(1) Å in $[\mathbf{Mn(hfac)_2}]_3\mathbf{(1)_2}$. The latter geometry generates poor orbital overlap, placing the S atom of one thiazyl ring between the S and N atoms of a neighboring ring, and thus poorly promotes AF coupling between thiazyl radical units. This type of geometric dependence of magnetic, as well as conductive, properties is well-known for related thiazyl radical systems.[34] In the case presented here, the result is that the S···

Table 1. Contact Distances and Geometries at 150 K

	S···S contact[a]				S···O contact A[b]			S···O contact B[b]		
complex	d (Å)	x (Å)	y (Å)	z (Å)	d (Å)	θ (deg)	φ (deg)	d (Å)	θ (deg)	φ (deg)
$[\mathbf{Mn(hfac)_2}]_3\mathbf{(1)_2}$	3.528(2)	0.46(1)	1.71(1)	3.05(1)	2.885(2)	67.6(1)	125.6(1)	3.102(2)	57.8(1)	114.2(1)
$[\mathbf{Mn(hfac)_2}]_3\mathbf{(2)_2}$[c]	3.388(2)	0.21(1)	1.72(1)	2.91(1)	2.915(3)	72.9(1)	127.5(1)	3.188(3)	60.8(1)	113.2(1)

[a]See Figure 2d for an illustration of the x, y, and z geometry parameters. [b]See panels a and b of Figure 2 for illustrations of the θ and φ geometry parameters. See Figure 2c for the definition of contacts A and B. [c]Information retrieved from the crystallographic information file (CIF) in the Cambridge Structural Database (CSD) (Refcode ACOHOR).[16]

O contacts should govern the magnetic properties, overriding contributions from the S···S contacts.

Magnetic Properties. The magnetic properties of $[\mathbf{Mn(hfac)_2}]_3\mathbf{(1)_2}$ were investigated between 300 and 1.8 K, at dc fields of 1000 and 10000 Oe, and at zero dc field with an oscillating ac field of 3 Oe at 150 Hz (Figure 4). At room

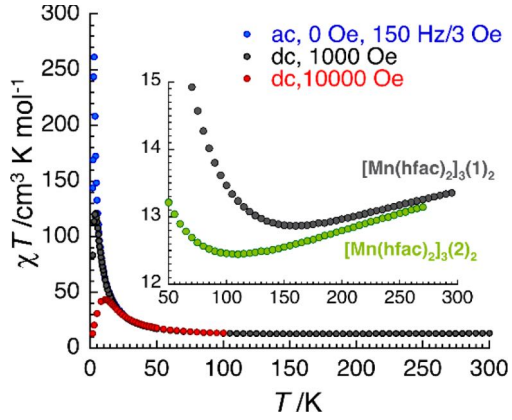


Figure 4. Temperature dependence of the χT product measured in dc (1000 and 10000 Oe dc fields) and ac (0 Oe dc field; 3 Oe oscillating ac field at a frequency of 150 Hz) modes with χ being the molar magnetic susceptibility equal to M/H for the dc measurements, and $\chi = \chi' = dM/dH$ for the ac measurements. The inset is a plot of χT vs T from 50 to 300 K for $[\mathbf{Mn(hfac)_2}]_3\mathbf{(1)_2}$ and $[\mathbf{Mn(hfac)_2}]_3\mathbf{(2)_2}$[16] at 1000 Oe.

temperature, the χT product is 13.4 cm^3 K mol^{-1}, in agreement with the expected value of 13.875 cm^3 K mol^{-1} in the presence of three $S = 5/2$ Mn(II) spin carriers (C = 4.375 cm^3 K mol^{-1}; $g = 2$) and two $S = 1/2$ radical ligands (C = 0.375 cm^3 K mol^{-1}; $g = 2$). When the temperature is decreased, the χT product decreases continuously to reach a minimum of 12.8 cm^3 K mol^{-1} at 160 K, indicating dominant antiferromagnetic (AF) coupling between Mn(II) and the radical ligand as previously observed for $[\mathbf{Mn(hfac)_2}]_3\mathbf{(2)_2}$,[16] and in agreement with an $S_T = 13/2$ ground spin state for the $[\mathbf{Mn(hfac)_2}]_3\mathbf{(radical)_2}$ molecules (Figure 3). Below 160 K, the χT product increases with a decrease in temperature, and below 20 K, the thermal behavior of the χT product becomes strongly field-dependent as expected for magnetic species with a large moment, which exhibit a rapid saturation of their magnetization at low temperatures. In a zero dc field (Figure 4), the χT product increases to 262 cm^3 K mol^{-1} at 3 K before a final decrease to 143 cm^3 K mol^{-1} at the lowest measurable temperature, 1.8 K. These χT values are well above the expected value for an $S_T = 13/2$ complex (24.375 cm^3 K mol^{-1}), indicating that intermolecular interactions are present in the crystal packing and favor a parallel alignment of the individual $[\mathbf{Mn(hfac)_2}]_3\mathbf{(1)_2}$ spins (Figure 3). This result contrasts remarkably with the observed antiparallel alignment of the $S_T = 13/2$ spins in $[\mathbf{Mn(hfac)_2}]_3\mathbf{(2)_2}$.[16] At this stage, the thermal behavior of the χT product is a clear indication of at least two different types of magnetic interactions: (i) antiferromagnetic within the $[\mathbf{Mn(hfac)_2}]_3\mathbf{(1)_2}$ complex observed above 160 K and similar to those of $[\mathbf{Mn(hfac)_2}]_3\mathbf{(2)_2}$ as shown in the inset of Figure 4 ($J_{Mn1-Rad}/k_B$ = −35 K and $J_{Mn2-rad}/k_B$ = −13 K with the following Hamiltonian: $H = -2J_{Mn1-Rad}[S_{Mn1}S_{rad} + S_{Mn1(ii)}S_{rad(ii)}] - 2J_{Mn2-Rad}\{S_{Mn2}[S_{rad} + S_{rad(ii)}]\}$)[16] and (ii) ferromagnetic-like [locally AF (Figure 3)] between the complexes through short pairwise S···O contacts along the chain (seen between 130 and 3 K).

The dc susceptibility magnetic data for the $[\mathbf{Mn(hfac)_2}]_3\mathbf{(1)_2}$ complex cannot be modeled adequately using the numerical approach taken for an isolated $[\mathbf{Mn(hfac)_2}]_3\mathbf{(radical)_2}$ complex.[16] The failure of this molecular model provides further evidence that intercomplex interactions are strongly relevant below 160 K (see the inset of Figure 4) and must be explicitly included to reproduce the experimental magnetic data. Therefore, the Heisenberg classical spin chain model was employed in the macrospin approximation ($k_BT \ll |J_{Mn1-Rad}|$ and $|J_{Mn2-rad}|$), as described by the following spin Hamiltonian:

$$\hat{H} = -2J\sum_{-\infty}^{+\infty}\vec{S}_{T,i}\vec{S}_{T,i+1} = -2J{S_T}^2\sum_{-\infty}^{+\infty}\vec{u}_i\vec{u}_{i+1} \quad (1)$$

where $\vec{u}_i$ is a unit vector and J is the magnetic interaction along the supramolecular chain between $S_T = 13/2$ macrospins. With effective ferromagnetic interactions ($J > 0$), the zero-field susceptibility, χ, presents a T^{-2} low temperature divergence.[35] This conclusion can be readily demonstrated using a relationship that is universally valid for any classical spin model:

$$\frac{\chi T}{C} = 2\frac{\xi}{a} = \sum_{-\infty}^{+\infty}\langle\vec{u}_i\vec{u}_{i+n}\rangle \quad (2)$$

where C is the Curie constant [$C = Ng^2\mu_B{}^2S_T(S_T + 1)/(3k_B)$ = 24.375 cm^3 K mol^{-1}], a is the cell parameter of the spin chain, ξ is the magnetic correlation length, and the sum terms $\langle\vec{u}_i\vec{u}_{i+j}\rangle = \Gamma^j$ are the correlation functions, with $\Gamma = \langle\vec{u}_i\vec{u}_{i+1}\rangle$ being the nearest neighbor correlation function. Using these notations, eq 2 can be simplified to

$$\frac{\chi T}{C} = \sum_{n=-\infty}^{n=+\infty}\Gamma^n = \frac{1+\Gamma}{1-\Gamma} \quad (3)$$

In the frame of the classical spin Heisenberg model, the correlation function Γ is expressed by

$$\Gamma = \coth\left(\frac{2JS_T^2}{k_BT}\right) - \left(\frac{k_BT}{2JS_T^2}\right) \quad (4)$$

In the zero-temperature limit, the coth term of Γ is close to unity and thus eq 3 simplifies to

$$\frac{\chi T}{C} = 2\frac{\xi}{a} \approx \frac{4JS_T^2}{k_BT} \quad (5)$$

As previously shown by Fisher for the Heisenberg classical spin chain model,[35] eq 5 illustrates the T^{-2} divergence of the chain susceptibility and the T^{-1} divergence of its associated correlation length. As shown in Figure 5, the experimental

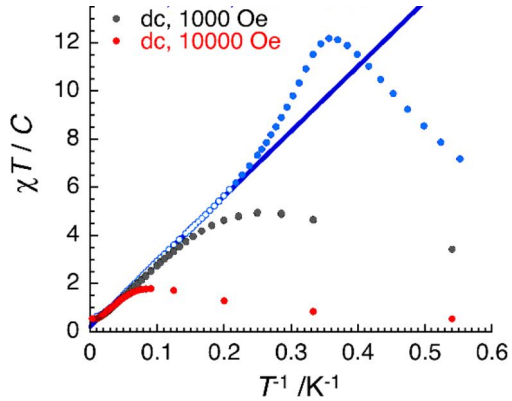


Figure 5. Plot of $\chi T/C$ vs $1/T$ data measured in dc (1000 and 10000 Oe dc fields) and ac (0 Oe dc field; 3 Oe oscillating ac field at a frequency of 150 Hz) modes. The best fit of ac data between 20 and 4.8 K to eq 5 is shown as a blue line.

χT product and thus the magnetic correlation length diverge with T^{-1} between 20 and 4.8 K with a prefactor equal to 27.1(5) K. The effective ferromagnetic interaction between S = 13/2 spins along the supramolecular chain (Figure 3) is estimated straightforwardly from eq 5 at J/k_B = 0.16 K. It is worth noting that the magnitude of this interaction is comparable to that observed in a similar isolated pairwise S···O interaction between two Mn(hfac)$_2$(radical) units in a previously investigated system.[11a] Thus, modeling of the susceptibility data (Figure 5 and eq 5) indicates an overall ferromagnetic-like interaction between the S_T = 13/2 complexes along [011], creating a Heisenberg ferromagnetic-like spin chain with only local AF spin−spin couplings. Nevertheless, the correlation length below 5 K (Figure 5) increases faster than the simple T^{-1} power law, suggesting an enhancement of the magnetic dimensionality and the influence of interchain magnetic interactions.

At 2.9 K, the zero-field χT product exhibits a clear maximum before decreasing to 1.85 K. Concomitantly, ac susceptibility measurements (Figure 6) reveal a non-zero out-of-phase component below 2.9 K, indicating the presence of slow magnetization dynamics. The very small frequency dependence (over 4 orders of magnitude) of the temperature at which the out-of-phase ac signal appears is characteristic of long-range ferro- or ferrimagnetic order with, here, a critical temperature, T_C, of 2.9 K. In this three-dimensional (3D) magnetically ordered phase, the magnetization increases in an applied dc field faster than a simple S = 13/2 Brillouin function without any step or anomaly that would suggest the presence of

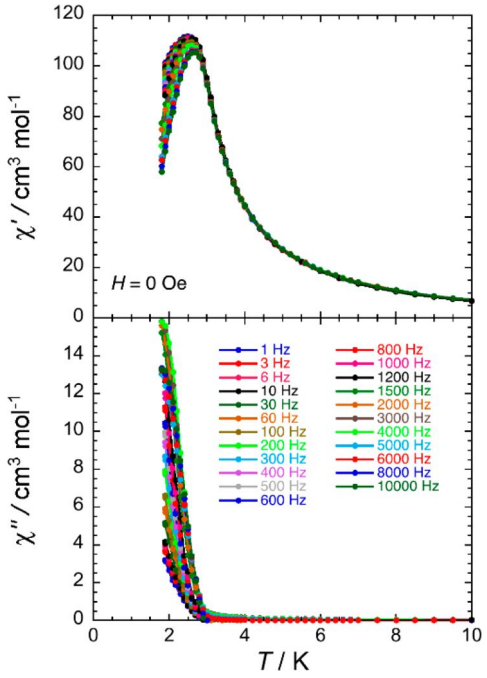


Figure 6. Temperature dependence of the ac susceptibility at different ac frequencies below 10 K in zero dc field: (top) in-phase component and (bottom) out-of-phase component.

interchain AF magnetic interactions (Figure S4). Quite remarkably, this magnetic behavior strongly suggests the presence of a ferrimagnetic state in $[\mathbf{Mn(hfac)_2}]_3\mathbf{(1)_2}$ below 2.9 K with only effective ferromagnetic interactions within and between the supramolecular S_T = 13/2 spin chains, while most likely only local AF interactions are present in the materials between S = 5/2 Mn(II) and S = 1/2 radical spins.

Coordination complexes $[\mathbf{Mn(hfac)_2}]_3\mathbf{(1)_2}$ and $[\mathbf{Mn(hfac)_2}]_3\mathbf{(2)_2}$ are structurally similar, with the methyl group positions being the major difference at the molecular level. In the solid state, the supramolecular structures exhibit small but important differences in distances and geometries of the reciprocal bifurcated (SS)···O contacts and the S···S contacts, the former being favored in $[\mathbf{Mn(hfac)_2}]_3\mathbf{(1)_2}$ and the latter being favored in $[\mathbf{Mn(hfac)_2}]_3\mathbf{(2)_2}$. These two competing contacts direct very different local magnetic interactions, the former favoring effective ferromagnetic coupling and the latter inducing antiferromagnetic ones between S_T = 13/2 complexes along the supramolecular chain (Figure 3). As a result, while $[\mathbf{Mn(hfac)_2}]_3\mathbf{(2)_2}$ exhibits magnetic properties consistent with a simple Heisenberg chain of antiferromagnetically coupled S_T = 13/2 spins,[16] $[\mathbf{Mn(hfac)_2}]_3\mathbf{(1)_2}$ displays a 3D ordered ferrimagnetic ground state at 2.9 K with S_T = 13/2 complexes in effective ferromagnetic coupling within and between Heisenberg spin chains.

We demonstrate that minor changes in the geometry of supramolecular contacts can dramatically alter the magnetic properties of a given system. This work highlights the subtlety of the local steric pressure that can influence the interplay between opposing local magnetic interactions. In the case presented here, chalcogen bonding is implicated in both the structural arrangement of the molecules in the solid state and

the local magnetic interactions that ultimately generate the 3D ferrimagnetic order. The local magnetic coupling enabled by chalcogen bonding competes with close contacts between radical ligands. The bulk magnetic properties of the material are dictated by which of the two competing interactions dominates and are thus dependent on the subtle but crucial difference in supramolecular geometry.

(1) Jeffrey, G. A.; Saenger, W. *Hydrogen Bonding in Biological Structures*; Springer-Verlag: Berlin, 1994.

(2) (a) Fersht, A. R. The hydrogen bond in molecular recognition. *Trends Biochem. Sci.* **1987**, *12*, 301−304. (b) Ariga, K.; Kunitake, T. Molecular Recognition at Air-Water and Related Interfaces: Complementary Hydrogen Bonding and Multisite Interaction. *Acc. Chem. Res.* **1998**, *31*, 371−378.

(3) Aakeröy, C. B.; Seddon, K. R. The hydrogen bond and crystal engineering. *Chem. Soc. Rev.* **1993**, *22*, 397−407.

(4) (a) Politzer, P.; Murray, J. S.; Clark, T. -Hole bonding: a physical interpretation. *Top. Curr. Chem.* **2014**, *358*, 19−42. (b) Wang, H.; Wang, W.; Jin, W. J. -Hole Bond vs –Hole Bond: A Comparison Based on Halogen Bond. *Chem. Rev.* **2016**, *116*, 5072−5104. (c) Cavallo, G.; Metrangolo, P.; Pilati, T.; Resnati, G.; Terraneo, G. Naming Interactions from the Electrophilic Site. *Cryst. Growth Des.* **2014**, *14*, 2697−2702.

(5) (a) Politzer, P.; Murray, J. S. Halogen bonding: an interim discussion. *ChemPhysChem* **2013**, *14*, 278−294. (b) Shields, Z. P.; Murray, J. S.; Politzer, P. Directional tendencies of halogen and hydrogen bonds. *Int. J. Quantum Chem.* **2010**, *110*, 2823−2832.

(6) Gilday, L. C.; Robinson, S. W.; Barendt, T. A.; Langton, M. J.; Mullaney, B. R.; Beer, P. D. Halogen Bonding in Supramolecular Chemistry. *Chem. Rev.* **2015**, *115*, 7118−7195.

(7) (a) Brezgunova, M. E.; Lieffrig, J.; Aubert, E.; Dahaoui, S.; Fertey, P.; Lebègue, S.; Ángyán, J. G.; Fourmigué, M.; Espinosa, E. Chalcogen Bonding: Experimental and Theoretical Determinations from Electron Density Analysis. Geometrical Preferences Driven by Electrophilic-Nucleophilic Interactions. *Cryst. Growth Des.* **2013**, *13*, 3283−3289. (b) Garrett, G. E.; Gibson, G. L.; Straus, R. N.; Seferos, D. S.; Taylor, M. S. Chalcogen bonding in solution: interactions of benzotelluradiazoles with anionic and uncharged Lewis bases. *J. Am. Chem. Soc.* **2015**, *137*, 4126−4133. (c) Ho, P. C.; Szydlowski, P.; Sinclair, J.; Elder, P. J. W.; Kübel, J.; Gendy, C.; Lee, L. M.; Jenkins, H. A.; Britten, J. F.; Morim, D. R.; Vargas-Baca, I. Supramolecular macrocycles reversibly assembled by Te···O chalcogen bonding. *Nat. Commun.* **2016**, *7*, 11299.

(8) Wang, W.; Ji, B.; Zhang, Y. Chalcogen bond: a sister noncovalent bond to halogen bond. *J. Phys. Chem. A* **2009**, *113*, 8132−8135.

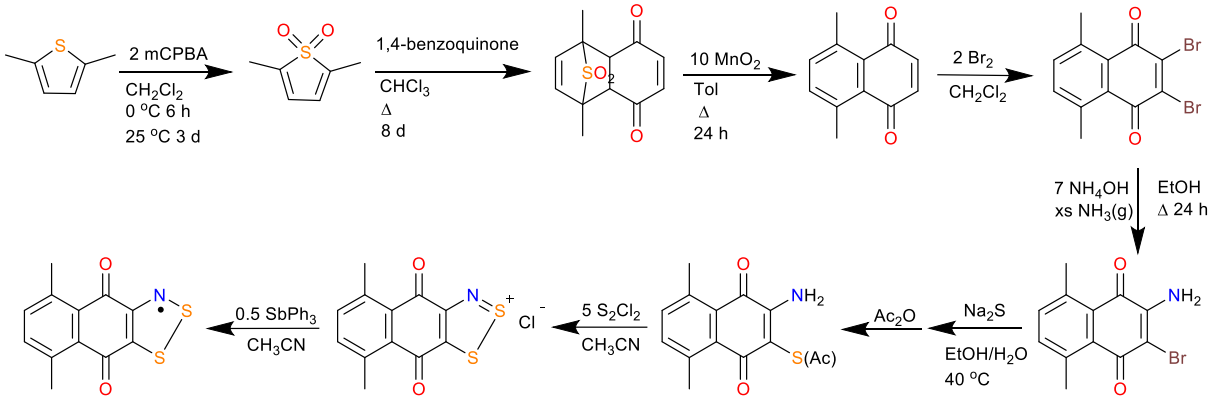
(9) Iwaoka, M.; Takemoto, S.; Tomoda, S. Statistical and Theoretical Investigations on the Directionality of Nonbonded S··· O Interactions. Implictions for Molecular Design and Protein Engineering. *J. Am. Chem. Soc.* **2002**, *124*, 10613−10620.

(10) (a) Thomas, S. P.; Jayatilaka, D.; Guru Row, T. N. S···O chalcogen bonding in sulfa drugs: insights from multipole charge density and X-ray wavefunction of acetazolamide. *Phys. Chem. Chem. Phys.* **2015**, *17*, 25411−25420. (b) Beno, B. R.; Yeung, K. S.; Bartberger, M. D.; Pennington, L. D.; Meanwell, N. A. A Survey of the Role of Noncovalent Sulfur Interacitons in Drug Design. *J. Med. Chem.* **2015**, *58*, 4383−4438. (c) Shukla, R.; Dhaka, A.; Aubert, E.; Vijayakumar-Syamala, V.; Jeannin, O.; Fourmigué, M.; Espinosa, E. Understanding Reactivity and Assembly of Dichalcogenides: Structural, Electrostatic Potential, and Topological Analyses of 3*H*-1,2-Benzodithiol-3-one and Selenium Analogs. *Cryst. Growth Des.* **2020**, *20*, 7704−7725.

(11) (a) Fatila, E. M.; Goodreid, J.; Clérac, R.; Jennings, M.; Assoud, J.; Preuss, K. E. High-spin supramolecular pair of Mn(II)/thiazyl radical complexes. *Chem. Commun.* **2010**, *46*, 6569−6571. (b) Wu, J.; MacDonald, D. J.; Clérac, R.; Jeon, I.-R.; Jennings, M.; Lough, A. J.; Britten, J.; Robertson, C.; Dube, P. A.; Preuss, K. E. Metal Complexes of Bridging Neutral Radical Ligands: pymDTDA and pymDSDA. *Inorg. Chem.* **2012**, *51*, 3827−3839. (c) Fatila, E. M.; Clérac, R.; Rouzières, M.; Soldatov, D. V.; Jennings, M.; Preuss, K. E. High-Spin Ribbons and Antiferromagnetic Ordering of a Mn^{II}-Biradical-Mn^{II} Complex. *J. Am. Chem. Soc.* **2013**, *135*, 13298−13301.

(12) Mayo, R. A.; Sullivan, D. J.; Fillion, T. A.; Kycia, S. W.; Soldatov, D. V.; Preuss, K. E. Reversible crystal-to-crystal chiral resolution: making/breaking non-bonding S···O interactions. *Chem. Commun.* **2017**, *53*, 3964−3966.

(13) Preuss, K. E. Pancake bonds: -Stacked dimers of organic and light-atom radicals. *Polyhedron* **2014**, *79*, 1−15.
(14) (a) Preuss, K. E. Metal-radical coordination complexes of thiazyl and selenazyl ligands. *Coord. Chem. Rev.* **2015**, *289*−*290*, 49−61. (b) Haynes, D. A. Crystal engineering with dithiadiazolyl radicals. *CrystEngComm* **2011**, *13*, 4793−4798. (c) Alberola, A.; Less, R. J.; Pask, C. M.; Rawson, J. M.; Palacio, F.; Oliete, P.; Paulsen, C.; Yamaguchi, A.; Farley, R. D.; Murphy, D. M. A thiazyl-based organic ferromagnet. *Angew. Chem., Int. Ed.* **2003**, *42*, 4782−4785.
(15) Fairhurst, S. A.; Johnson, K. M.; Sutcliffe, L. H.; Preston, K. F.; Banister, A. J.; Hauptman, Z. V.; Passmore, J. Electron spin resonance study of $CH_3CNSSN^{\bullet}$, $C_6H_5CNSSN^{\bullet}$, and S NSSN$^{\bullet+}$ free radicals. *J. Chem. Soc., Dalton Trans.* **1986**, 1465−1472.
(16) Sullivan, D. J.; Clérac, R.; Jennings, M.; Lough, A. J.; Preuss, K. E. Trinuclear Mn(II) complex with paramagnetic bridging 1,2,3-dithiazolyl ligands. *Chem. Commun.* **2012**, *48*, 10963−10965.
(17) Britten, J.; Hearns, N. G. R.; Preuss, K. E.; Richardson, J. F.; Bin-Salamon, S. Mn(II) and Cu(II) Complexes of a Dithiadiazolyl Radical Ligand: Monomer/Dimer Equilibria in Solution. *Inorg. Chem.* **2007**, *46*, 3934−3945.
(18) Torssell, K.; Dyrnum, O. S.; Lindstrom, B.; Schaumburg, K.; Vialle, J.; Anthonsen, T. Diels-Alder Reactions of Thiophene Oxides Generated in situ. *Acta Chem. Scand.* **1976**, *30b*, 353−357.
(19) Connelly, N. G.; Geiger, W. E. Chemical Redox Agents for Organometallic Chemistry. *Chem. Rev.* **1996**, *96*, 877−910.
(20) (a) O'Brien, D. A.; Duling, D. R.; Fann, Y. C. *WinSim Public EPR Software Tools, MS-Windows 9x*, NT version 0.98; National Institute of Environmental Health Sciences, 2002. (b) Duling, D. R. Simulation of multiple isotropic spin-trap EPR spectra. *J. Magn. Reson., Ser. B* **1994**, *104*, 105−110.
(21) *CrysAlisPro Software*, version 1.171.35.8; Agilent Technologies, 2011.
(22) Sheldrick, G. M. A short history of *SHELX*. *Acta Crystallogr., Sect. A: Found. Crystallogr.* **2008**, *64*, 112−122.
(23) Sheldrick, G. M. Crystal structure refinement with *SHELXL*. *Acta Crystallogr., Sect. C: Struct. Chem.* **2015**, *71*, 3−8.
(24) Schön, G.; Hopf, H. Alkine und Cumulene, XIII. Diels-Alder-Additionen von Doppelbindungsdienophilen an konjugierte Bisallene. *Liebigs Ann. Chem.* **1981**, *1981*, 165−180.
(25) (a) Bailey, D.; Williams, V. E. An efficient synthesis of substituted anthraquinones and naphthoquinones. *Tetrahedron Lett.* **2004**, *45*, 2511−2513. (b) Iguchi, K.; Sugihara, Y.; Nakayama, J. Preparation of Sterically Congested Compounds: 6,7-Di-*t*-butyl-1,4-naphthoquinone, 2,3,6,7-Tetra-*t*-butylanthraquinone, and 2,3,6,7-Tetra-*t*-butylanthracene. *Bull. Chem. Soc. Jpn.* **2008**, *81*, 304−306. (c) Bailey, D.; Murphy, J. N.; Williams, V. E. From enolates to anthraquinones. *Can. J. Chem.* **2006**, *84*, 659−666.
(26) Mashraqui, S.; Keehn, P. Active MnO_2. Oxidative Dehydrogenations. *Synth. Commun.* **1982**, *12*, 637−645.
(27) Wurm, G.; Schwandt, S. Methylated 2-aryl-1,4-naphtoquinone derivatives with diminished antioxidative activity. *Pharmazie* **2003**, 531−538.
(28) Buckle, D. R.; Smith, H.; Spicer, B. A.; Tedder, J. M. Studies on v-triazoles. 9. Antiallergic 4,9-dihydro-4,9-dioxo-1H-naphtho[2,3-d]-v-triazoles. *J. Med. Chem.* **1983**, *26*, 714−719.
(29) Warburton, W. K. Arylthiazathiolium Salts and *o*-Aminoaryl Thiols - The Herz Reaction. *Chem. Rev.* **1957**, *57*, 1011−1020.
(30) Smithson, C. S.; MacDonald, D. J.; Matt Letvenuk, T.; Carello, C. E.; Jennings, M.; Lough, A. J.; Britten, J.; Decken, A.; Preuss, K. E. A 1,2,3-dithiazolyl-*o*-naphthoquinone: a neutral radical with isolable cation and anion oxidation states. *Dalton Trans.* **2016**, *45*, 9608−9620.
(31) Steed, K. M.; Steed, J. W. Packing Problems: High Z' Crystal Structures and Their Relationship to Cocrystals, Inclusion Compounds, and Polymorphism. *Chem. Rev.* **2015**, *115*, 2895−2933.
(32) Fatila, E. M.; Mayo, R. A.; Rouzières, M.; Jennings, M. C.; Dechambenoit, P.; Soldatov, D. V.; Mathonière, C.; Clérac, R.; Coulon, C.; Preuss, K. E. Radical-Radical Recognition: Switchable Magnetic Properties and Re-entrant Behavior. *Chem. Mater.* **2015**, *27*, 4023−4032.
(33) Rosenfield, R. E., Jr.; Parthasarathy, R.; Dunitz, J. D. Directional preferences of nonbonded atomic contacts with divalent sulfur. 1. Electrophiles and nucleophiles. *J. Am. Chem. Soc.* **1977**, *99*, 4860−4862.
(34) (a) Leitch, A. A.; Lekin, K.; Winter, S. M.; Downie, L. E.; Tsuruda, H.; Tse, J. S.; Mito, M.; Desgreniers, S.; Dube, P. A.; Zhang, S.; Liu, Q.; Jin, C.; Ohishi, Y.; Oakley, R. T. From Magnets to Metals: The Response of Tetragonal Bisdiselenazolyl Radicals to Pressure. *J. Am. Chem. Soc.* **2011**, *133*, 6051−6060. (b) Brusso, J. L.; Clements, O. P.; Haddon, R. C.; Itkis, M. E.; Leitch, A. A.; Oakley, R. T.; Reed, R. W.; Richardson, J. F. Bistability and the Phase Transition in 1,3,2-Dithiazolo[4,5-*b*]pyrazin-2-yl. *J. Am. Chem. Soc.* **2004**, *126*, 14692−14693. (c) Fujita, W.; Awaga, K. Room-Temperature Magnetic Bistability in Organic Radical Crystals. *Science* **1999**, *286*, 261−262.
(35) Fisher, M. E. Magnetism in One-Dimensional Systems - The Heisenberg Model for Infinite Spin. *Am. J. Phys.* **1964**, *32*, 343−346.



Scheme S1. Preparative procedure for **1**; mCPBA = *m*-chloroperbenzoic acid

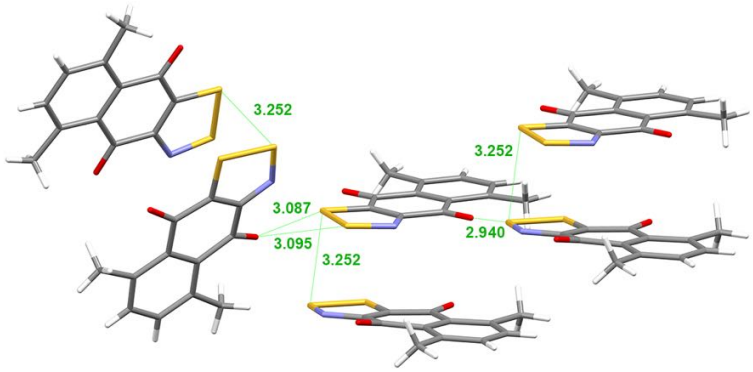


Figure S1. Excerpt of the crystal structure of **1α** illustrates that the short S···O contacts occur between twisted cofacial pancake-bonded dimers (distances given in Ångstroms).

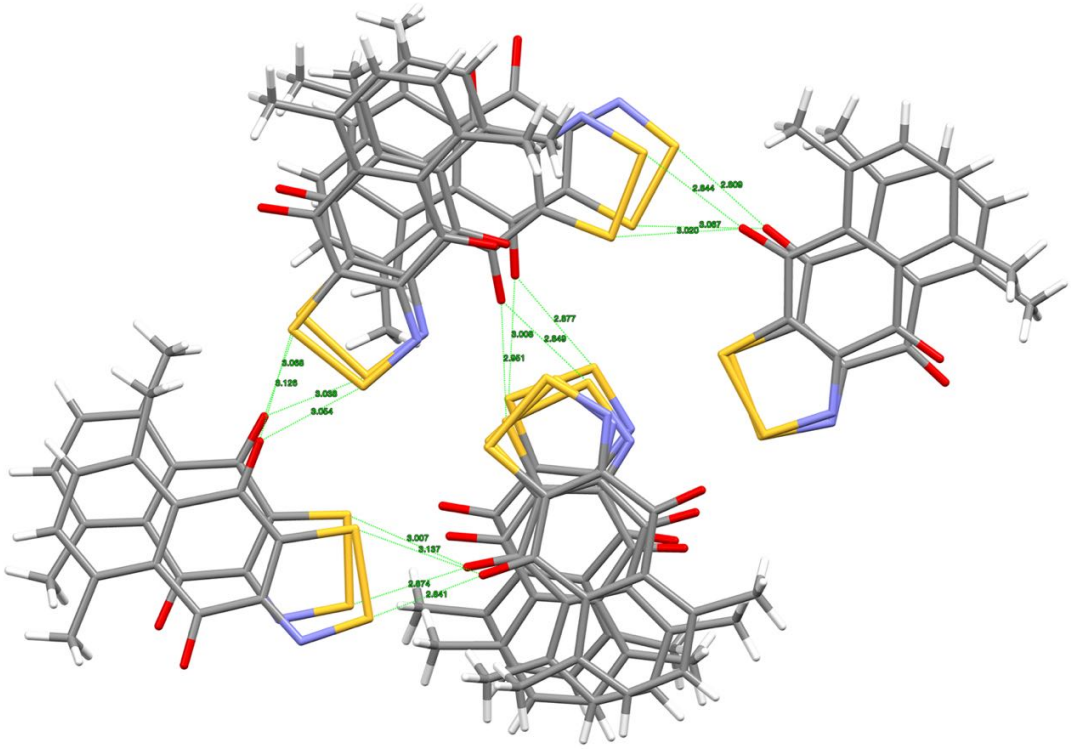


Figure S2. Excerpt of the crystal structure of **1β** shows all twelve molecules in the asymmetric unit, arranged as six independent cis-cofacial pancake-bonded dimers. Geometry of overlap between thiazyl rings is not ideal. Short S···O contacts only occur within the asymmetric unit, not between asymmetric units (distances in Ångstroms).

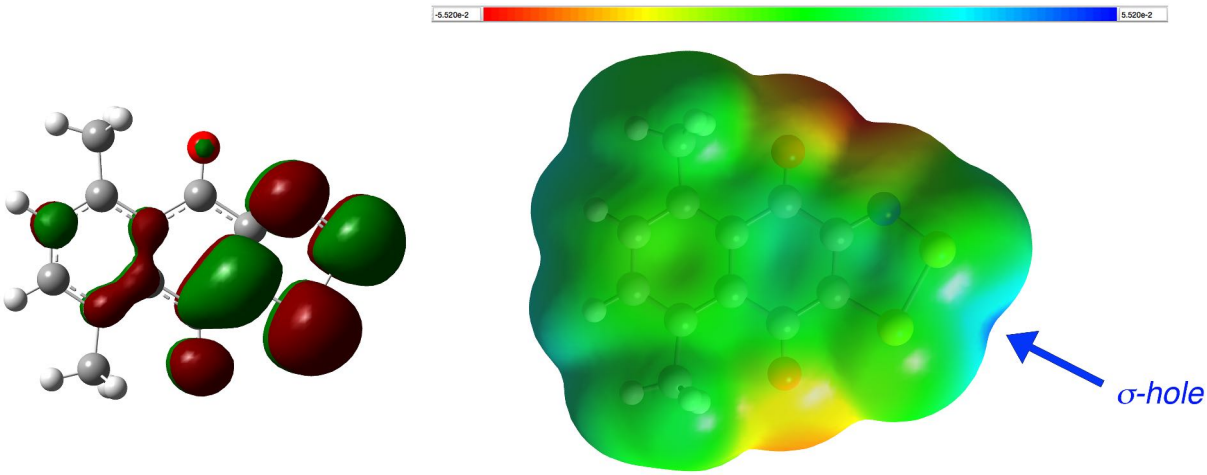


Figure S3. (left) Singly occupied molecular orbital (SOMO) of **1** calculated using uB3LYP/6-311G**; (right) Electrostatic Potential (ESP) surface of **1** calculated from same.

Table S1. Summary of single crystal X-ray diffraction analyses

Crystal	**1α**	**1β**	**$[Mn(hfac)_2]_3(1)_2$**
Molecular formula	$C_{12}H_8NO_2S_2$	$C_{12}H_8NO_2S_2$	$C_{54}H_{22}F_{36}Mn_3N_2O_{16}S_4$
FW (g mol^{-1})	262.31	262.31	1931.79
Crystal system	monoclinic	triclinic	triclinic
Space group	$P2_1/n$	P-1	P-1
Temperature (K)	293(2)	293(2)	150(1)
Radiation	CuK_α	CuK_α	MoK_α
Radiation wavelength (Å)	1.54184	1.54184	0.71073
Unit cell lengths (Å) a b c	 8.06550(17) 7.88825(15) 34.3000(7)	 16.9500(3) 17.0055(4) 23.4667(5)	 11.4539(3) 12.8715(3) 13.3873(2)
Unit cell angles (°) α β γ	 90 93.1726(19) 90	 86.6531(17) 81.9008(17) 78.7462(18)	 115.3383(19) 92.5796(18) 93.895(2)
V (Å^3)	2178.91(8)	6564.6(2)	1773.66(7)
Z'	2	12	0.5
Z	8	24	1
Density – calculated (g cm^{-3})	1.599	1.592	1.809
Absorption coefficient (mm^{-1})	4.334	4.316	0.803
F(000)	1080	3240	951
Crystal size (mm^3)	0.50 × 0.03 × 0.03	0.10 × 0.10 × 0.10	0.33 × 0.06 × 0.02
θ range for data collection (°)	5.166 to 75.605	3.312 to 70.319	2.919 to 29.574
Index ranges	h, -10/10 k, -9/9 l, -43/41	h, -20/19 k, -20/14 l, -28/28	h, -15/15 k, -17/17 l, -18/18
Reflections collected	6520	44568	35541
Independent reflections	6520 (R_{int} = 0.0680)	24706 (R_{int} = 0.0411)	9930 (R_{int} = 0.0328)
Completeness (%)	100.0% to θ = 67.684°	98.7% to θ = 67.684°	99.6% to θ = 25.242°
Absorption correction	Semi-empirical from equivalents	Semi-empirical from equivalents	Semi-empirical from equivalents
Refinement method	Full-matrix least squares on F^2	Full-matrix least squares on F^2	Full-matrix least squares on F^2
Data / restraints / parameters	6520 / 0 / 312	24706 / 0 / 1861	9930 / 330 / 598
Goodness-of-fit on F^2	1.047	0.982	1.066
Final R indices [$I > 2\theta(I)$]	$R1$ = 0.0461 $wR2$ = 0.1297	$R1$ = 0.0528 $wR2$ = 0.1450	$R1$ = 0.0418 $wR2$ = 0.0974
R indices (all data)	$R1$ = 0.0502 $wR2$ = 0.1320	$R1$ = 0.0668 $wR2$ = 0.1504	$R1$ = 0.0560 $wR2$ = 0.1031
Final min/max (e Å^{-3})	-0.360 / +0.310	-0.423 / +0.942	-0.524 / +0.743
CCDC deposition #	1559406	1559407	1559408

Magnetic measurements

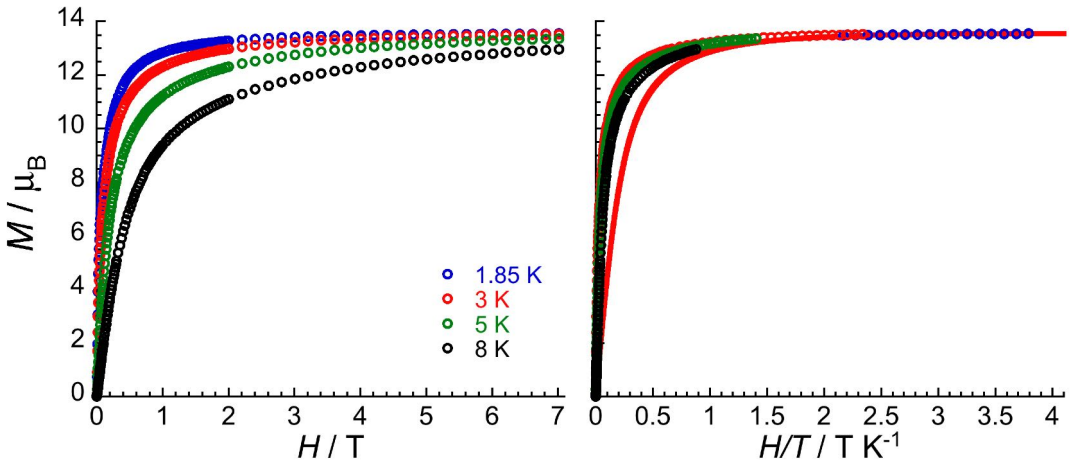


Figure S4. Field dependence of the magnetization, *M*, for **[Mn(hfac)$_2$]$_3$(1)$_2$** below 8 K plotted as (left) *M* vs *H* and (right) *M* vs *H*/*T* plots. The solid red line is the best fit of the *M* vs *H*/*T* plots above 4 T to an *S* = 13/2 Brillouin function as discussed in the main text. It shows that experimental magnetization saturation occurs more quickly than the *S* = 13/2 Brillouin function, indicative of additional effective ferromagnetic interactions between S_T = 13/2 units.